Available online at www.sciencedirect.com
ScienceDirect
Catalysis Today 131 (2008) 35–41
CATALYSIS TODAY
www.elsevier.com/locate/cattod

Coral-like nanostructured α-Mn_2O_3 nanaocrystals for catalytic combustion of methane
Part I. Preparation and characterization

Yi-Fan Han *, Luwei Chen, Kanaparthi Ramesh, Ziyi Zhong, Fengxi Chen, Jianhau Chin, Hongwai Mook

Institute of Chemical and Engineering Sciences, 1 Pesek Road, Jurong Island 627833, Singapore

Available online 26 November 2007

Abstract

Coral-like nanostructured α-Mn_2O_3 nanocrystals were prepared by oxidative decomposition of $MnCO_3$, exhibiting tremendous activity in the catalytic combustion of methane. This prepared α-Mn_2O_3 nanocrystals showed ultra-high stability during reaction while the structure feature was unaffected. The ultra-stable structure of the α-Mn_2O_3 catalyst has been demonstrated by characterization of SEM, XPS, XRD, Raman spectroscopy. The performance of the α-Mn_2O_3 nanocrystals has proven reproducible and potentially to be an applied catalyst for methane combustion.

Keywords: Methane combustion; α-Mn_2O_3; Catalyst; Coral-like nanostructure; Characterization

1. Introduction

Catalytic combustion of methane over metal oxides [1,2] and Pd-based catalysts [3] has been widely studied over past decades due to its attractive potential for industrial applications, e.g., burning turbines fuelled by natural gas, since single methane molecule contains one carbon and gives off the lowest amount of CO_2 (green-house gas) when it is completely oxidized comparing with other hydrocarbons. More recently, with the growth of natural gas fuelled vehicles the strict law has been made for the abatement of methane emission, since methane is known as a flammable gas, also contributing to green-house effect [4]. In the future, on the other hand, methane combustion is still a vital process in the removal of gas mixture from coal mine [5], which has been regarded as a recoverable energy [6].

Manganese oxides (MnO_x) and its mixtures with other oxides (MnO_x–M_xO_y: M = V, Cr, Co, Fe, Cu, Zr, etc.) [2,5–14] have proven highly active, durable and low cost catalysts for completely oxidizing various volatile organic substances or hydrocarbons long before. However, MnO_x-based catalysts have several inherent disadvantages compared to supported Pd catalysts in applications, e.g., (i) relatively low activity and high light-off temperature, (ii) difficult to reproduce the structure of mixed oxide catalyst by most of preparing methods currently developed. Interestingly, single crystalline MnO_x has been found to exhibit remarkable activity towards some oxidation reactions in comparison with multivalent manganese oxides, e.g., Mn_2O_3 in the deep oxidation of ethylene [15] and methane [5], decomposition of NO_x [16], and MnO_2 in benzene combustion [17] and ammonia oxidation [18]. However, synthesizing single crystalline MnO_x having high activity and stability in the oxidation reaction, especially for those reactions at high temperatures, e.g. >500 °C, is of great challenge.

Presently, nanosized MnO_x crystals are regarded as a promising alternative for this application. In the recent past, controllable synthesis of MnO_x nanomaterials has attracted considerable attentions from both academia and industry [19–21]. Among them, MnO_x nanocrystals with various morphologies or porous structure, e.g., nanoarrays, nanowires, and nanospheres, have been developed [22,23]. Unfortunately, due to the facile phase-transformation of MnO_x, during preparation only multivalent manganese oxides (MnO_2, Mn_2O_3 and

* Corresponding author.
E-mail address: han_yi_fan@ices.a-star.edu.sg (Y.-F. Han).

0920-5861/$ – see front matter © 2007 Elsevier B.V. All rights reserved.
doi:10.1016/j.cattod.2007.10.016

Mn_3O_4) are usually produced in those supported and unsupported nanoparticles. Recently, we have successfully synthesized Mn_2O_3 and Mn_3O_4 nanocrystals by thermolysis of manganese(II, III) acetylacetonate using mesoporous SBA-15 as template, it has proved to be active towards CO oxidation below 250 °C [24–25]. Nevertheless, unsupported MnO_x nanoparticles were found to sinter and aggregate strongly during catalytic combustion. Thus, preparation of Mn_2O_3 nanocrystals having considerable activity and stability for catalytic combustion of methane is highly desirable.

In the present study, a nanostructured α-Mn_2O_3 with coral-like feature is prepared by oxidative decomposition of a commercial $MnCO_3$. The activity of α-Mn_2O_3 as-prepared is measured during total oxidation of low concentration methane (0.5%). Peluso et al. [26] has reported that the Mn_2O_3 catalyst produced by this method showed significant reactivity in the complete oxidation of ethanol. However, the unique feature of Mn_2O_3 and its surface modification during reaction have not been addressed so far. Thus, efforts in this work have been made for investigating the surface structure of the nanocomposites Mn_2O_3 affected by reactants during methane combustion. For this propose, the structure of all fresh and spent catalysts is characterized by scanning electronic microscopy (SEM), X-ray diffraction (XRD), X-rays photon spectroscopy (XPS), and laser Raman spectroscopy (LRS). For comparison, a commercial α-Mn_2O_3 catalyst was also studied in all experiments.

2. Experimental

2.1. Catalyst preparation and reactivity measurements

α-Mn_2O_3 nanocrystals were prepared by a direct thermal decomposition of $MnCO_3$ powder (Aldrich, batch no. 13520DD) in static air. Calcination of high purity of $MnCO_3$ powder was carried out at 500, 700, 850 and 900 °C, respectively, with a ramping rate of 1 °C/min for 5 h.

Activity measurements were carried out in a micro-plug-flow reactor. Prior to each experiment, the dried α-Mn_2O_3 catalyst was pretreated in situ by heating in 20 ml/min of Ar flow at 50 °C for 2 h. The temperature-dependant reactivity was carried out in a stream of 0.5% CH_4, 3.0% O_2 and helium with space velocity of 36,000 h^{-1} under atmospheric pressure. The analysis of the reactant was done with an online GC (Shimadzu GC-2010) in equipped with a CP-carbonBOND column. For comparison, a commercial α-Mn_2O_3 (Aldrich, 99.999%, 4.8 m^2/g) was tested under the same conditions.

2.2. Characterization

LRS. The dispersive Raman microscope employed in this study was a JY Horiba LabRAM HR equipped with three laser sources (UV, visible, and NIR), a confocal microscope, and a liquid nitrogen cooled charge-coupled device (CCD) multi-channel detector (256 pixels × 1024 pixels). The visible 514.5 nm argon ion laser was selected to excite the Raman scattering. The laser power from the source is around 20 mW, but when it reached the samples, the laser output was reduced to around 6–7 mW after passing through filtering optics and microscope objective. A 100× objective lens was used and the acquisition time for each Raman spectrum was approximately 60–120 s depending on the sample. The Raman shift range acquired was in the range of 200–1200 cm^{-1} with spectral resolution 1.7–2 cm^{-1}.

XRD. X-ray diffraction patterns were obtained with a Bruker D8 diffractometer using Cu Kα radiation (λ = 1.540589 Å). The crystal size particles size of MnO_x was calculated with the width of diffraction profiles, referring to the full width of half maximum (FWHM) of crystalline phase at ⟨2 2 2⟩, ⟨4 4 0⟩ and ⟨6 2 2⟩ using Debye–Scherrer formula:

$$D = \frac{0.9 \times \lambda}{\Delta \times \cos(\theta)} \quad (1)$$

where D: crystal size, λ: wavelength of X-rays, Δ: FWHM of diffraction peak, θ: angle corresponding to the peak.

N_2 adsorption. The surface area of catalyst was obtained from the adsorption and desorption N_2 isotherms that were collected on Autosorb-6 at liquid N_2 temperature. Prior to the measurement, all samples were degassed at 300 °C until a stable vacuum of ca. 5 mTorr was reached.

SEM. The measurements were performed at JEOL JSM-6700F Field Emission SEM. About 200 particles were selected when the average particle size was estimated based on SEM images.

XPS. The surface was analyzed by XPS that was performed on a VG ESCALAB 250 spectrometer, using Al-K_α radiation (1486.6 eV, pass energy 20.0 eV). The base pressure of the instrument is 1×10^{-9} Torr. The background contribution B (E) (obtained by shirley method) caused by inelastic process was subtracted, while the curve-fitting was performed with Gaussia–Lorentzian profile by an standard software. The binding energies (BEs) were calibrated using C 1s peak at 85.0 eV. The instrument was also calibrated by using Au wire. XPS spectra were recorded at $\theta = 90°$ of X-ray sources.

TPO (temperature-programmed-oxidation). Prior to the TPO experiments, a commercial MnO (Aldrich, 99.99%, 1.1 m^2/g), Mn_2O_3 (Aldrich, 99.999%, 4.8 m^2/g) were pretreated in Ar at 323 K in a flow rate of 30 ml/min for 2 h to remove excess moisture and carbonaceous impurities. Experiments of TPO were performed in a micro fixed-bed reactor, which is connected to GC-QMS (HPR-20, Hiden Analytical Ltd.); while masses (*m/e*: 2, 16, 18, 28, 32 and 44) were monitored, and the detection limits in Ar are 100 ppm for CO, 10 ppm for CO_2 and H_2, and less than 1 ppm for O_2. The temperature was increased from 50 to 625 °C with a linear heating (1 °C/min) in a carrier gas of O_2 (5.0 kPa + Ar) of 50 ml/min for TPO. Meanwhile, thermogravimetric analysis (TGA) of $MnCO_3$ was performed on a Setaram Setsys Evolution 12, with a flow rate of 20 ml/min N_2 and a ramping rate of 5 °C/min.

3. Results and discussion

The TGA analysis of $MnCO_3$ was shown in Fig. 1. Loss of ca. 10% weight was seen in curve A when heating from room

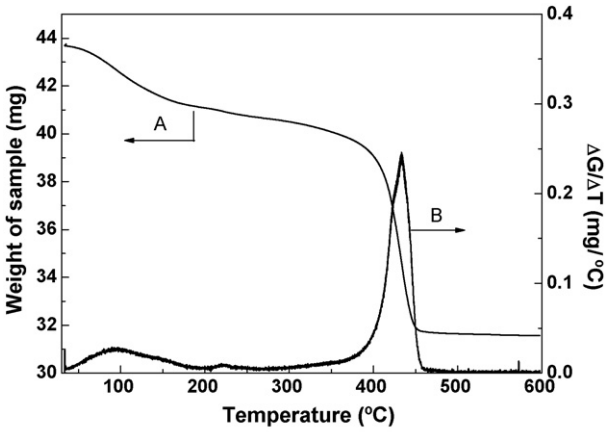

Fig. 1. TGA profile for $MnCO_3$. A: the weight of sample vs. temperature, B: the rate of weight loss as a function of temperature.

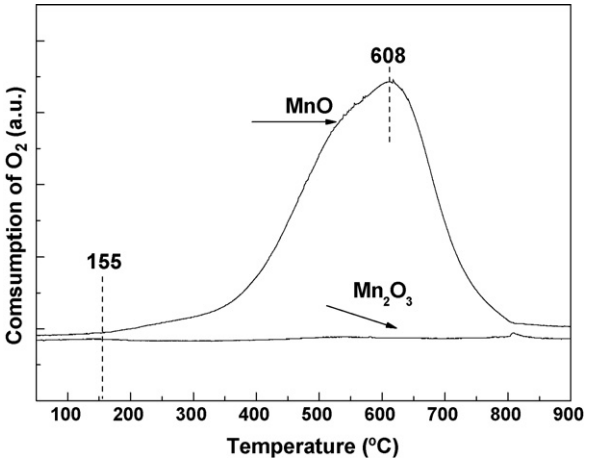

Fig. 2. TPO spectra for commercial bulk MnO and Mn_2O_3.

temperature to 350 °C, it may be due to the desorption of physically adsorbed water on $MnCO_3$ surface. With further increasing the temperature $MnCO_3$ was decomposed rapidly in the range of 400–450 °C as indicated by curve B. Complete decomposition was observed at ca. 450 °C. The main products should be CO_2 and MnO because the thermolysis of $MnCO_3$ was conducted in an oxygen-free atmosphere. By in situ XRD analysis Peluso et al. [26] found that $MnCO_3$ was not decomposed until to 300 °C in an oxygen flow, agreeing well with our observations. On the other hand, as shown in Fig. 2, the profile of TPO is due to the fact that the oxidation of bulk MnO to Mn_2O_3 starts at 155 °C, and ceases at 827 °C after surpassing a maxima peak at 608 °C [24]. In contrast, bulk Mn_2O_3 was very stable under the same conditions. Those results indicate that the decomposition of $MnCO_3$ and oxidation of MnO may occur simultaneously under our preparing conditions. Therefore, in order to fully transfer $MnCO_3$ to Mn_2O_3 the oxidative decomposition in this study was performed at or above 500 °C.

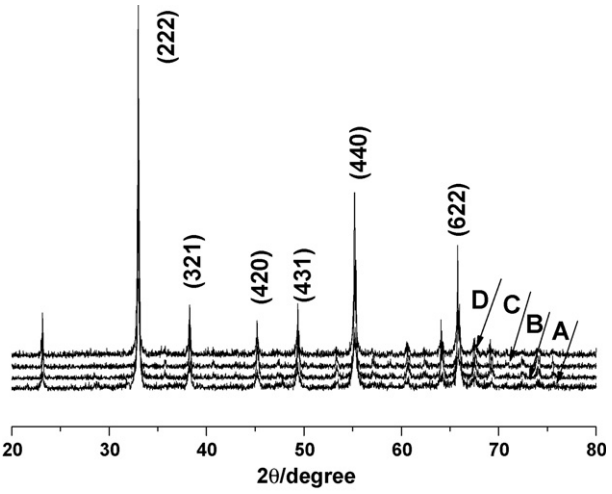

Fig. 3. XRD patterns for the nanostructured α-Mn_2O_3 prepared by oxidative decomposition at 500 °C (A), 700 °C (B), 850 °C (C) and a commercial bulk Mn_2O_3 (D).

First of all, we investigated the Mn_2O_3 morphology affected by the calcination temperatures via decomposing $MnCO_3$ at 500, 700, and 850 °C in static air, respectively. As shown in Fig. 3, the powder XRD patterns prove that all products exhibit the same structure corresponding to the typical bixbyite α-Mn_2O_3 (JCPDS 41-1442), which is identical with the pattern obtained for the commercial Mn_2O_3. The average particle size was calculated by the Debye–Scherrer formula (Eq. 1) based on

Table 1
Textural properties of nanostructured α-Mn_2O_3

Samples from different calcination temperature	Crystallite phase	Crystal size (nm)		Surface area (m^2/g)
		XRD	SEM	
500 (°C)				
Unreacted	α-Mn_2O_3	31.0	35.0	40.0
Reacted[a]		40.0	42.0	35.5
700 (°C)				
Unreacted	α-Mn_2O_3	50.0	52.0	19.0
Reacted[a]		50.0	53.0	18.5
850 (°C)				
Unreacted	α-Mn_2O_3	150.0	155.0	5.0
Reacted[a]		153.0	155.0	5.0
900 (°C) unreacted	α-Mn_2O_3, Mn_3O_4	~300		4.0

[a] The catalyst was preformed in the stream of 0.5% CH_4, 3.0% O_2, rest He, space velocity: 36,000 h^{-1}, at 550 °C for 10 h.

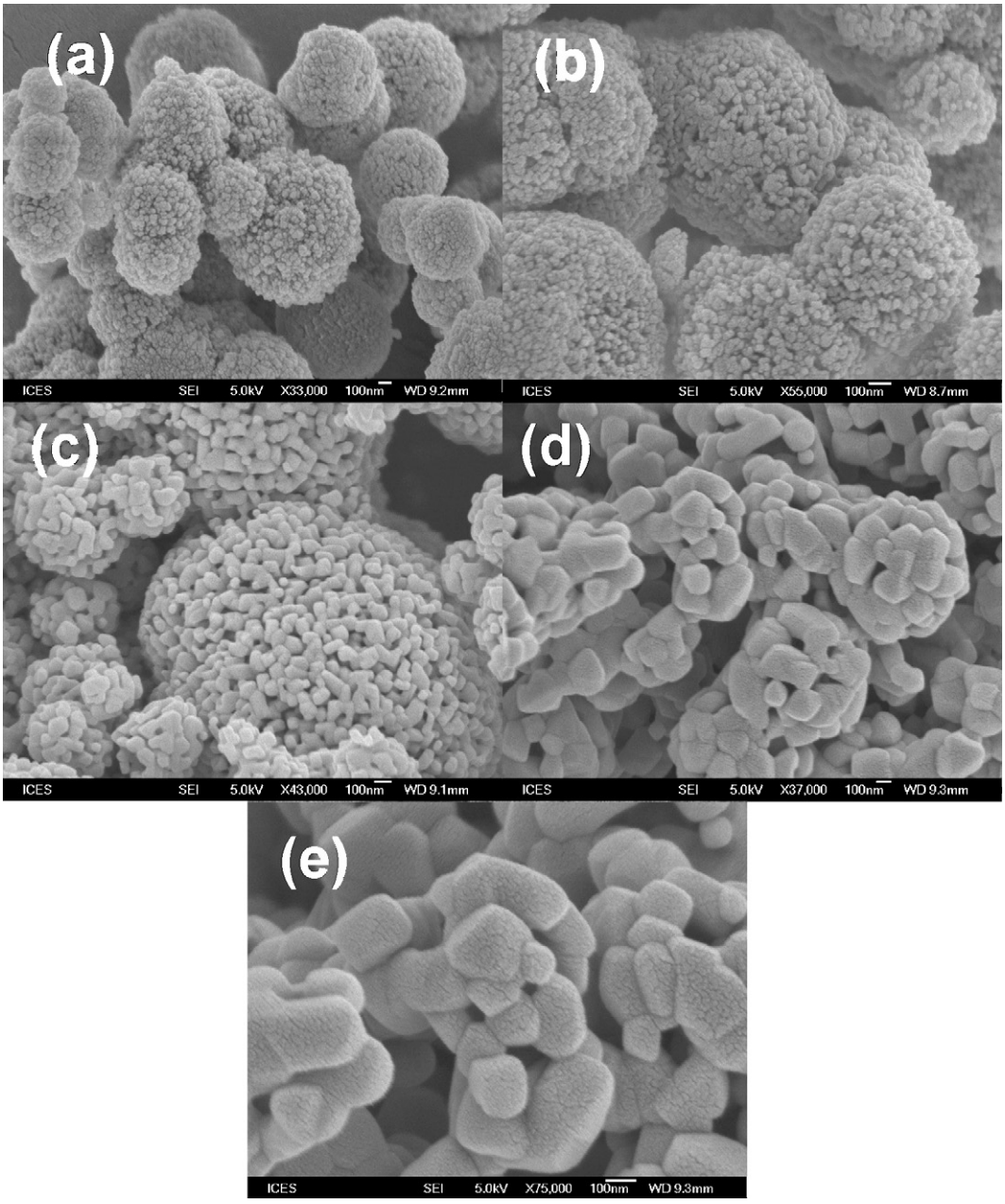

Fig. 4. SEM images recorded for the precursor $MnCO_3$ (a) and nanostructured α-Mn_2O_3 prepared by oxidative decomposition at 500 °C (b), 700 °C (c), 850 °C (d) and 900 °C (e).

the main reflection peaks at ⟨2 2 2⟩, ⟨4 4 0⟩ and ⟨6 2 2⟩. As listed in Table 1, the particle size is ca. 31.0 nm at 500 °C, and reaches to 50.0 nm at 700 °C and 150.0 nm at 850 °C, respectively. The mild increase of the particle size is due to the sintering and aggregation at elevated temperatures. Meanwhile, surface area of α-Mn_2O_3 dropped down rapidly from 40.0 m^2/g at 500 °C to 19.0 m^2/g at 700 °C, and further down to 5.0 m^2/g at 850 °C. In addition, Peluso et al. [26] observed the $2\theta = 32.4^\circ$ for ⟨2 2 2⟩ and 37.6° for ⟨3 2 1⟩ in XRD patterns of the MnO_x from oxidative decomposition of $MnCO_3$, deviation of ca. 0.8° from the pure α-Mn_2O_3, which indicated that the MnO_x thus prepared might be mainly composed of α-Mn_2O_3 accompanying with a tiny amount of γ-MnO_2 when heating in the temperature range of 400–500 °C. Moreover, previous studies have also revealed that the transformation of γ-MnO_2 to α-Mn_2O_3 can occur only above ca. 500 °C [27–28]. Therefore, it is understandable that only α-Mn_2O_3 was produced in our experiments, since the $2\theta = 33.2^\circ$ and 38.4° were detected for all samples as seen in XRD patterns in Fig. 3. Actually, the particle size evaluated from XRD for all samples are very close to that visualized from SEM, as displayed in Table 1.

SEM images in Fig. 4 show that the uniform α-Mn_2O_3 particles obtained from $MnCO_3$ (Fig. 4a) pile up to form a coral-like structure in a nest-shape with voids inside. The unique structure was kept up to 850 °C, as shown in Fig. 4b (500 °C), 4c (700 °C) and 4d (850 °C). The generation of Mn_3O_4 was observed when the calcination temperature was greater than 900 °C. It is consistent with the general transition

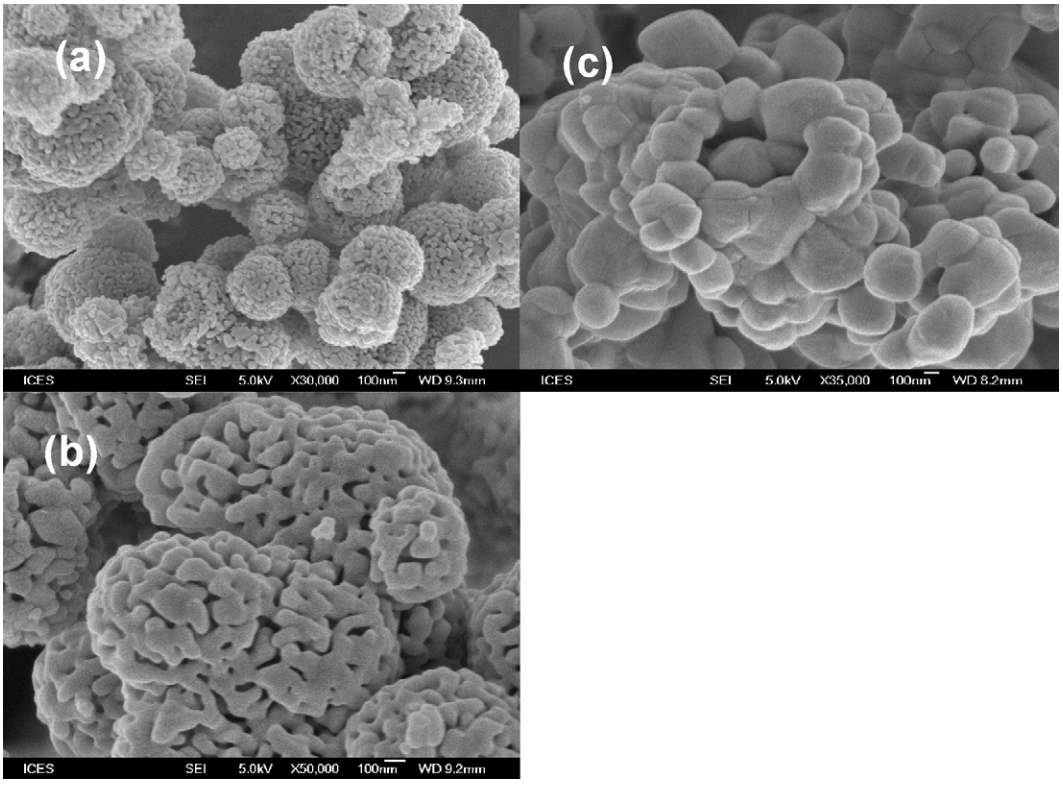

Fig. 5. SEM images recorded for the nanostructured α-Mn_2O_3 after methane combustion. Catalyst prepared by oxidative decomposition at 500 °C (a), 700 °C (b) and 850 °C (c). Reaction conditions: in the stream of 0.5% CH_4, 3.0% O_2, rest He, space velocity: 36,000 h^{-1} at 550 °C for 10 h.

temperatures of MnO_x as previously reported [29]: $Mn_2O_3 \overset{900°C}{\longrightarrow} Mn_3O_4 \overset{1700°C}{\longrightarrow} MnO$. In addition, the nest structure collapsed when the calcination temperature was above 900 °C, see Fig. 4e. It should be noted that discussing the performance of Mn_3O_4 in methane combustion is beyond the scope of present study. After reaction (550 °C for 10 h), we found a mild growth of the particles for the catalyst from the calcination at 500 °C (Fig. 5a); there were almost no change for the spent catalysts from the calcinations at 700 °C (Fig. 5b) and 850 °C (Fig. 5c).

In order to get insights into the structural modifications of the catalysts during reaction, the variation of crystalline phases and Mn valences were further determined using LRS and XPS spectroscopy in the case of the catalyst from the calcination at 700 °C. The LRS spectra obtained for the fresh and spent catalysts under ambient circumstance are shown in Fig. 6. The bands at 310, 365, 640 and 697 cm^{-1} detected for the bulk MnO_x may correspond to the out-of-plane bending modes of Mn_2O_3, asymmetric stretch of bridge oxygen species (Mn–O–Mn), symmetric stretch of Mn_2O_3 groups, respectively [30–33]. Taking a close look at these spectra, we found that those peaks were almost not broadened or shifted after reaction, an indicative that the nanoparticles structure was quite stable under reaction conditions and were unlikely affected by the reactants. However, note that the minor modifications of the structure during the reaction cannot be rule out, this study is underway.

On the other hand, surplus information of Mn chemical states was acquired from the XPS analysis. Currently, a great number of studies have been contributed to detect the Mn–O system by using XPS [34–38]. Unfortunately, the variation of XPS binding energies of Mn 2p alone, from Mn^{2+} to Mn^{4+}, usually is too small (less than ca. 1.0 eV) to precisely evaluate the Mn valence in manganese oxides (MnO_x). So, the analysis of XPS results from all catalysts was conducted by comparing with the spectra from a commercial bulk α-Mn_2O_3 and also referring the previous studies. As displayed in Fig. 7, the binding energy (BE) of $Mn2p_{3/2}$ for the α-Mn_2O_3 (calcination at 700 °C) is ca 641.9 eV before reaction and ca. 642.0 eV after

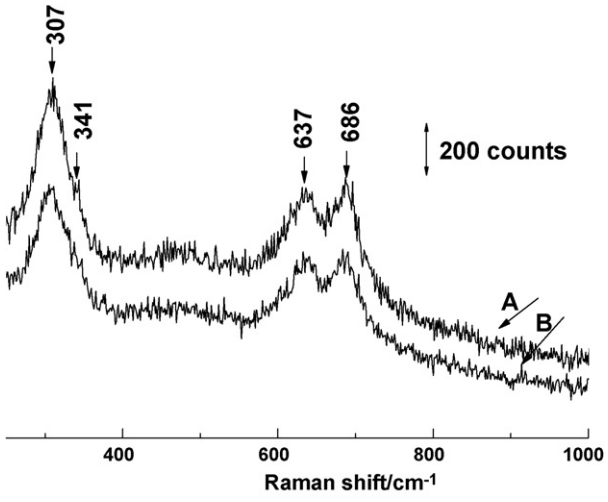

Fig. 6. Raman spectra for the catalyst as-prepared at 700 °C: (A) unreacted, (B) reacted as the same conditions in Fig. 5.

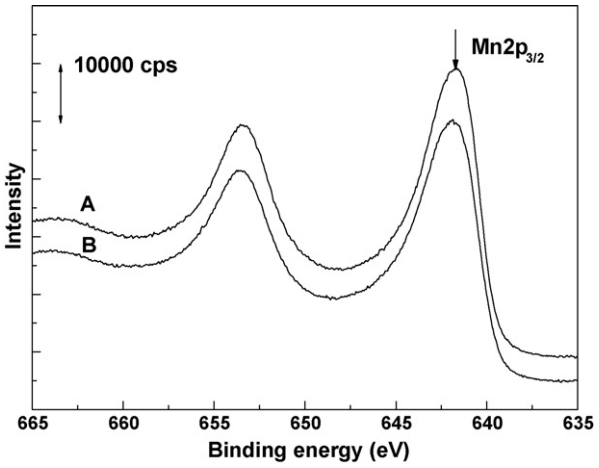

Fig. 7. XPS of Mn 2p spectra for the catalyst as-prepared at 700 °C: (A) unreacted, (B) reacted as the same conditions in Fig. 5.

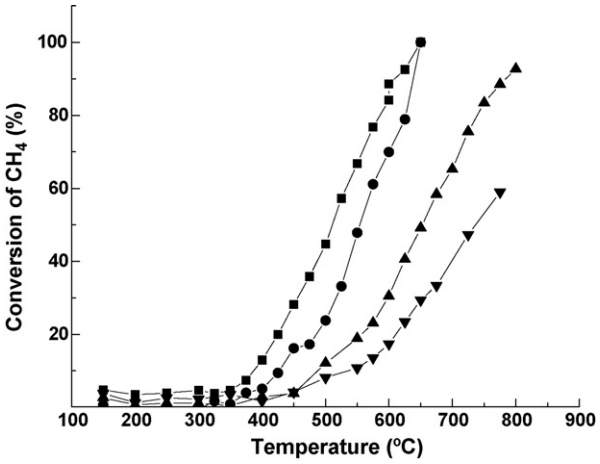

Fig. 9. Catalytic activity of the nanostructured α-Mn_2O_3 catalyst prepared by oxidative decomposition at 500 °C (■), 700 °C (●), 850 °C (▼) and a bulk Mn_2O_3 (▲).

reaction, approaching to 641.8 eV observed for the commercial sample. In addition, the extent of Mn 3s multiplet splitting measured simultaneously (Mn 3sΔ*E*) offers additional insights into the Mn chemical states. The Mn 3sΔ*E* is ca. 5.3 eV obtained for the fresh and used catalysts, see Fig. 8. Compared to results reported in the literature [24–25], Mn^{3+} should be the dominant species on the surface. The values of Mn 3sΔ*E* (eV) and Mn 2p and the LRS spectra suggest that the Mn chemical states are little affected, or to say, the surface structure is very stable during methane combustion.

Fig. 9 shows that the conversion of methane increases with increasing the reaction temperature above ca. 400 °C for all catalysts. The temperature for the full conversion of methane can be above 600 °C. Comparatively, the light-off temperature (defining at 20% conversion of methane) is 423, 486, and 556 °C for the α-Mn_2O_3 calcined at 500, 700 and 850 °C. The decrease of the reactivity with the rise of calcination temperature is possible due to the decrease of surface area of α-Mn_2O_3. In contrast, the commercial α-Mn_2O_3 (Aldrich, 99.9% of purity, 4.0 m^2/g of surface area and average size of 0.5 μm) shows the light-off temperature only at 613 °C. On the other hand, the coral-like α-Mn_2O_3 catalyst also showed high stability for this reaction. For instance, loss of 2.0% of the initial activity was observed for the α-Mn_2O_3 calcined at 700 °C after running for 24 h.

In this context, we have demonstrated that the prepared α-Mn_2O_3 nanocrystals have excellent performance for methane combustion. The high reactivity and durability have been associated with the unique coral-like nanostructure of the α-Mn_2O_3 that was derived from oxidative combustion of $MnCO_3$. This unique structure is believed to have capability to prevent the grain α-Mn_2O_3 from aggregation during the reaction. It has been proved that the surface area (BET) of as-prepared α-Mn_2O_3 changed little during reaction. There is no phase-transformation for the spent catalyst as evidenced by XRD. The comparison of Raman and XPS spectra obtained from the fresh and used catalysts indicated that the Mn chemical states was likely unaffected during the reaction. More kinetic studies as well as the surface modification during methane combustion over this novel nancrystal α-Mn_2O_3 catalyst is undergoing in our group.

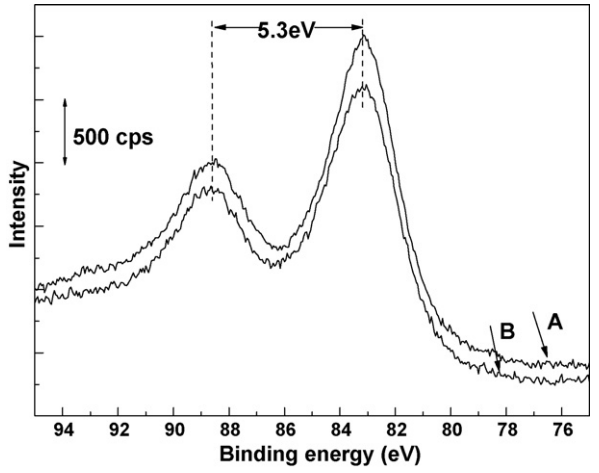

Fig. 8. XPS of Mn 3s spectra for the catalyst as-prepared at 700 °C: (A) unreacted, (B) reacted as the same conditions in Fig. 5.

4. Conclusions

In this study, a coral-like α-Mn_2O_3 catalyst has been prepared through the oxidative decomposition of $MnCO_3$. Thus prepared catalyst showed very high reactivity and durability in the combustion of methane. SEM showed that the morphology of coral-like α-Mn_2O_3 catalyst remained after reaction. And the bulk surface structure of α-Mn_2O_3 nanocrystal was also not changed as XRD and LRS, while XPS spectra revealed that Mn^{3+} was the only Mn chemical states in the surface. This nanocomposite can be a potentially applied catalyst for complete methane combustion.

Acknowledgment

We are pleased to acknowledge the financial support by ICES, A*Star, Singapore.

References

[1] M.F.M. Zwinkels, S.G. Jaras, P.G. Menon, Catal. Rev. Sci. Eng. 35 (1993) 319.
[2] A.J. Zarur, J.Y. Ying, Nature 403 (2000) 65.
[3] D. Ciuparu, M.R. Lyubovsky, E. Altman, L.D. Pfefferle, A. Datye, Catal. Rev. Sci. Eng. 44 (2002) 593.
[4] R.J. Charlson, Nature 438 (2005) 165.
[5] R.B. Anderson, K.C. Stein, J.J. Feenan, L.J.E. Hofer, Ind. Eng. Chem. 53 (1961) 809.
[6] J.R. Rostrup-Nielson, Catal. Rev. Sci. Technol. 46 (2004) 247.
[7] H.M. Zhang, Y. Teraoka, N. Yamazoe, Catal. Today 6 (1989) 155.
[8] D.L. Trim, Appl. Catal. 7 (1984) 249.
[9] J.J. Spivery, Ind. Eng. Chem. Res. 26 (1987) 2165.
[10] J.J. Spivery, J.B. Butt, Catal. Today 11 (1992) 465.
[11] J.R. Kittrell, J.W. Eldrige, W.C. Connor, Catalysis 9 (1991) 162.
[12] M.I. Zaki, M.A. Hasan, L. Pasupulety, N.E. Fouad, H. Knözinger, New J. Chem. 23 (1999) 67.
[13] R. Radhakrishnan, S.T. Oyama, J. Catal. 199 (2001) 282.
[14] D. Döbber, D. Kieβling, W. Schmitz, G. Wendt, Appl. Catal. B 52 (2004) 135.
[15] B. Dmuchovsky, M.C. Freerks, F.B. Zienty, J. Catal. 4 (1965) 577.
[16] T. Yamashita, A. Vannice, Appl. Catal. B: Environ. 13 (1997) 141.
[17] A. Naydenov, D. Mehandjiev, Appl. Catal. A: Gen. 97 (1993) 17.
[18] N.I. Il'Chenko, G.I. Golodets, J. Catal. 39 (1975) 57.
[19] S.L. Brock, .N. Duan, Z.Y. Tian, O. Giraldo, H. Zhou, S.L. Suib, Chem. Mater. 10 (1998) 2619.
[20] M. Fernandez-Garcia, A. Martinez-Arias, J.C. Hanson, J.A. Rodriguez, Chem. Rev. 10 (2004) 4063.
[21] Y. Xiong, Y. Xie, Z. Li, C. Wu, Chem. Eur. J. 9 (2003) 1645.
[22] B. Tian, X. Liu, H. Yang, S. Xie, C. Yu, B. Tu, D.Y. Zhao, Adv. Mater. 15 (2003) 1370.
[23] V. Escax, M. Imperor-Clerc, D. Bazin, A. Davidson, C. R. Chimie 8 (2005) 663.
[24] Y.-F. Han, F. Chen, Z.-Y. Zhong, K. Ramesh, E. Widjaja, L.-W. Chen, Catal. Commun. 7 (2006) 739.
[25] Y.-F. Han, F. Chen, Z.-Y. Zhong, K. Ramesh, L.-W. Chen, E. Widjaja, J. Phys. Chem. B 110 (2006) 24450.
[26] M.A. Peluso, J.E. Sambeth, H.J. Thomas, React. Kinet. Catal. Lett. 80 (2003) 241.
[27] M. Lamaita, M.A. Peluso, J.E. Sambeth, H.J. Thomas, Appl. Catal. B: Environ. 61 (2005) 128.
[28] S. Kanungo, J. Catal. 58 (1979) 419.
[29] E.R. Stobbe, B.A. de Boer, J.W. Genus, Catal. Today 47 (1999) 161.
[30] Y.T. Chua, P.C. Stair, I.E. Wachs, J. Phys. Chem. B 105 (2001) 8600.
[31] M.-C. Bernard, A.H. Goff, B.V. Thi, S.C. De Torresi, J. Electrochem. Soc. 140 (1993) 3065.
[32] J.M. Chalmers, P.R. Riffiths (Eds.), Handbook of Viberational Spectroscopy, Jim Wilkie, J&R Press, UK, 2002.
[33] F. Buciuman, F. Patcas, R. Cracium, D.R.T. Zahn, Phys. Chem. Chem. Phys. 1 (1999) 185.
[34] L.Z. Zhao, V.J. Young, Electron Spectrosc. Relat. Phenom. 34 (1984) 45.
[35] J. van Elp, R.H. Potze, H. Eskes, R. Berger, G.A. Sawatzky, Phys. Rev. B 44 (1991) 1530.
[36] V.D.I. Castro, G. Polzonetti, J. Electron. Spectrosc. Relat. Phenom. 48 (1989) 117.
[37] S.D. Gardner, G.R. Hoflund, M.R. Davidson, Langmuir 7 (1991) 2140.
[38] T. Grzybek, J. Klinik, M. Rogoz, H. Papp, J. Chem. Soc., Faraday Trans. 94 (1998) 2843.